Fast electron damage mechanism of epoxy resin studied by electron energy loss spectroscopy and electron diffraction

Jun Kikkawa,[1, a)] Aoi Nii,[2,] Yoshiaki Sakaniwa[3], Naochika Kon[2], Marina Sakamaki[3], Touyou Ohashi[3], Nobuyasu Nita[2], Koji Harano[1] and Koji Kimoto[1]

[1]National Institute for Materials Science, 1-1 Namiki, Tsukuba 305-0044, Japan

[2]Mitsubishi Materials Corporation, 1002-14 Mukohyama, Naka 311-0102, Japan

[3]Mitsubishi Materials Corporation, 1-600 Kitabukuro, Omiya, Saitama 330-8508, Japan

[a)]Electronic address: KIKKAWA.Jun@nims.go.jp

ABSTRACT

The damage mechanism and exposure tolerance of epoxy resins to fast electrons remain unclear. We quantitatively investigated the effects of electron irradiation on a common epoxy resin by dose-dependent electron energy loss spectroscopy (EELS). The results show that sp^3 states of nitrogen, oxygen, and their adjacent carbon atoms were converted to sp^2 states, forming imine (C=N) and carbonyl (C=O) as the total electron dose increased. The sp^3 to sp^2 conversion mechanism was proposed. The epoxy resin was very sensitive to fast electrons and the original electronic states were maintained up to a

total dose of ~10^3 e^- nm^{-2} at a low temperature of 103 K. Dose-dependent electron diffraction (ED) revealed that the intra- and intermolecular geometries changed below and around the total dose of ~10^3 e^- nm^{-2}.

I. INTRODUCTION

Epoxy resins are widely used in the current industry for materials such as adhesives, coating ingredients, and encapsulants owing to their characteristics such as excellent thermal and mechanical properties, chemical resistance, and moldability.[1] They are applied not only in our daily environment but also in the space environment where durability to cosmic rays is required.[2] Epoxy resins are generally made through chemical reactions of epoxy compounds (or base resins) with curing agents (or hardeners).[3] Although their chemical reactions and polymerized network structures are important to understand because they affect the physical properties of epoxy resins, they are not fully understood and are the subject of intense research.[3, 4] From a functional viewpoint, in addition to their macroscopic physical properties, it is also important to understand the microscopic properties of epoxy resins, such as chemical bonding states at heterointerfaces in adhesion.[5] In space, it is also important to understand the resistance of

epoxy resins to cosmic rays (protons, helium nuclei, electrons, etc., with near-light speed) and the damage mechanisms.[2]

Electron microscopy, a powerful microscopic characterization method, has recently enabled the analysis of polymetric materials sensitive to electron beams, owing to advances in measurement techniques and detector performance.[6, 7] We expect that measuring the chemical bonding states of epoxy resins at the atomic to nanometer scale in specific areas, such as heterointerfaces in adhesion, by electron energy loss spectroscopy (EELS) in electron microscopes will open the way to gaining a new scientific understanding of epoxy resins. However, the resistance of epoxy resin to fast electrons of 30–300 keV (i.e., common energies used in electron microscopy) and the mechanism of how and which part of the epoxy resin is damaged remain unclear, although there have been some previous studies.[8-11]

In this study, we use 300 keV electrons (~78 % of the speed of light) in an electron microscope and quantitatively investigate the effects of electron irradiation on a cured epoxy resin by EELS with a high detective quantum efficiency (DQE) camera. From the results for carbon, nitrogen, and oxygen *K* edges and the 1–35 eV region in EELS, we identify the essential nature of the damage and propose a mechanism of its formation in the epoxy resin. Durability, i.e., the maximum total electron dose that maintains the

electronic states, for the epoxy resin is also elucidated. By electron diffraction (ED), we also found that molecular geometry changes occur before electronic state changes at the initial stage of irradiation.

II. EXPERIMENTAL METHOD

We used *N*,*N*,*N*',*N*'-tetraglycidyl-4,4'-methylenedianiline (TGMDA) (Tokyo Chemical Industry Co.) as a base resin and 2-ethyl-4-methylimidazole (2E4MZ) (Shikoku Chemicals Co.) as a curing agent, and mixed them in a molar ratio of 22.5:4.5 [Fig. 1(a)]. The mixture was applied to surface-treated aluminum and heated at 180°C for 1 h in the atmosphere to obtain an epoxy resin. The possible chemical reactions of TGMDA with 2E4MZ are shown in Fig. 1(b). 2E4MZ acts as a ring-opening initiator on the oxirane of TGMDA to form an alkoxide, which reacts with an oxirane of another TGMDA monomer to open the ring. Repeated ring-opening and chain growth through reactions between the alkoxide and oxirane of TGMDA initiate polymerization.[3] The detachment of the 2E4MZ moiety and rebonding by heating ultimately result in a cured epoxy resin having a backbone structure composed of benzenoid and side-chain parts, as shown in Fig. 1(b).

A microtome (Leica EM UC7 Ultramicrotome, Leica Microsystems GmbH) was used to prepare thin cross-sectional specimens of the cured epoxy resin coated on aluminum

for EELS. We used a monochromated electron microscope (Themis Z, Thermo Fisher Scientific, Inc.) with a spectrometer (Quantum 970, Gatan Inc.) and a high DQE complementary metal-oxide-semiconductor (CMOS)-based direct electron detection camera (K2 IS, Gatan Inc.) for electron dose-dependent EELS. All the data presented in this paper were obtained using 300 keV electrons. The specimen was set on a cooling holder (Elsa, Gatan Inc.). The specimen temperatures with and without liquid nitrogen in the microscope were 103 K and 303 K, respectively. For electron dose-dependent EELS, we used a parallel electron beam with a diameter of 216 nm, electron flux j ($\times 10^4$ e^- nm^{-2} s^{-1}) values of 0.84 and 3.19, energy dispersions of 0.025 eV/ch (in Sec. III-A and III-D) and 0.1 eV/ch (in Sec. III-C), and convergence and collection semi-angles of ~0 mrad and 6 mrad. Prior to the dose-dependent EELS, we determined the measurement positions and stored their coordinates with a very small j. Then, after blanking the electron beam, we set j to either 0.84 or 3.19 by adjusting a condenser lens to a premeasured value. Moving to the measurement position, we started the repeated acquisition of a single EELS spectrum with each exposure time Δt. After starting the repetitive EELS, the specimen was exposed to the electron beam at time t_0. Denoting the start time of the i-th EELS as t_i and the number of acquisitions of a single spectrum as n_f, we define the total electron dose D_e for the i-th EELS as $D_e = j\left(t_i + n_f \Delta t/2 - t_0\right)$. Δt and n_f were 0.2 s and 2–8 for a high

loss region (i.e., 280 eV–580 eV in Sec. III-A–III-C), and 4.9 ms and 10 for a low loss region (i.e., less than 35 eV in Sec. III-D). In Sec. III-D, we collected 4×10^4 EELS spectra from unirradiated positions in a 1 μm×1 μm area with Δt=4.9 ms using a beam scan mode to obtain a single spectrum with a high signal-to-noise ratio by integrating those spectra. The flux j was estimated to be ~0.01. Both the convergence and collection semiangles were set to 16 mrad. The thickness of the measurement areas was calculated to be 80–90 nm, using the standard log-ratio method.[12] In Sec. III-E, we also describe dose-dependent ED at 103 K using 300 keV electrons, an electron flux of 8.07 e^- nm^{-2} s^{-1} (j =8.07×10^{-4}), a selected area of 4.45 μm diameter, an exposure time Δt of 1.2768 s for single ED and another CMOS-based camera (One View, Gatan Inc.) mounted on the microscope. Denoting the start time of the i-th ED as t_i and the exposure time of the single ED as Δt, we can write the total electron dose D_e for the i-th ED as $D_e = j(t_i + \Delta t/2 - t_0)$, similar to the case of EELS.

III. RESULTS AND DISCUSSION

A. Dose-dependent EELS for carbon *K* edge at 303 K and 103 K

Figure 2 shows the dose dependence of the carbon *K* edge at 303 K and 103 K, where the electron flux j (×10^4 e^- nm^{-2} s^{-1}) was set to 0.84 for the dose D_e (×10^4 e^- nm^{-2} s^{-1}) of

0.16–13.6 and to 3.19 for D_e of 21.0–953. The combination of spectra obtained with two different j in Fig. 2 is appropriate because the flux dependence of the electron beam damage in the epoxy resin was small and the dose is an important parameter in describing the degree of damage. In Figs. 2(a) and 2(b), the series of spectra obtained with the same j have the same y-axis scale. There are clear differences in the carbon K edge profiles between 303 K and 103 K, as shown in Fig. 2. Because carbon is the main element in the epoxy resin, the damage mechanism and postdamage structure are significantly different between 303 K and 103 K. When D_e =0.16, the carbon K edge has a sharp peak at 285.3 eV (peak A), characterized by 1s→π* excitations at both 303 K and 103 K. The position of peak A shifts ~0.5 eV from 285.3 eV at D_e =0.16 to ~284.8 eV at D_e =953 for both temperatures. For 303 K in Fig. 2(a), an additional intensity at ~286.7 eV (labeled B) is observed at D_e >21, making peak A appear to broaden toward the higher energy loss side with increasing D_e. For 103 K in Fig. 2(b), two additional peaks appear at 287.4–287.6 eV (labeled C) when $D_e \geq 1.5$ and at 286.6–286.7 eV (labeled B) when $D_e \geq 21$, where peak B is more clearly observed than at 303 K. Peaks B and C also shift ~0.1 eV to the lower energy loss side in the range $1.5 \leq D_e \leq 953$, and ~0.2 eV in the range $21 \leq D_e \leq 953$ respectively, as D_e increases in Fig. 2(b). In the energy loss region of 288–293 eV, a steplike profile is observed only when D_e =0.16 at 103 K [Fig. 2(b)], and the variations in

the EELS profile for $0.83 \leq D_e \leq 953$ at 103 K are similar to those for $0.16 \leq D_e \leq 953$ at 303 K. Peaks B and C, i.e., the presence of two energetically localized unoccupied states for 103 K, suggest that the carbon atoms in the epoxy resin reconstruct two stable chemical bonds under electron irradiation, while they reconstruct chemical bonds in a disordered manner at 303 K. It is known that the primary damage process, i.e., inelastic scattering with molecular excitation, ionization, and collective molecular excitation, is dominant at low temperatures and causes molecular vibrations and the breaking of bonds such as C-H and C-C.[13] As the specimen temperature increases, secondary processes, i.e., the thermal diffusion of bond-broken atoms such as H atoms, the cross-linking of molecular chains, and the evaporation of atoms and molecules, affect the polymer structure.[13] The difference in the carbon *K* edge variation in Fig. 2 is attributed to the greater and lesser effects of the secondary processes at 303 K and 103 K, respectively. In the following, we focus on the irradiation effects at 103 K, because the carbon *K* edge for $D_e = 0.16$ has fine structures that probably reflect the original electronic structure, and there is approximately only one primary damage process to be considered.

B. Carbon K edge at low total dose

Figure 3 shows the same EELS spectrum for D_e =0.16 as in Fig. 2(b) with the reference EELS spectra of aniline and diethyl ether in the vapor phase[14, 15] and their linear combination for comparison. The carbon *K* edge of the cured epoxy resin reflects the linear combination of the EELS for the benzenoid part and the EELS for the side-chain part, as shown in Fig. 1(b). To ensure that the spectrum for D_e =0.16 in Fig. 2(b) reflects the original state, we roughly assume that the carbon *K* edges of the benzenoid and side-chain parts are those for aniline and diethyl ether, respectively, and compare the carbon *K* edge for the epoxy resin obtained with D_e =0.16 at 103 K and a linear combination of the carbon *K* edges for aniline and diethyl ether. The spectrum for aniline shows four π* peaks at 285.2 eV, 286.7 eV, 289.0 eV, and 290.5 eV as a result of the dominant excitations of 1s (C_{bz}-H) → π* (e_{2u}), 1s (C_{bz} -N_{sp^3}) → π* (e_{2u}), 1s (C_{bz}-H) → π* (b_{2g}), and 1s (C_{bz} -N_{sp^3}) → π* (b_{2g}) and two broad σ* peaks at 294.5 eV and 302 eV, respectively, in Fig. 3.[14, 16, 17] The subscripts 'bz' and 'sp^3' denote the atom in the benzenoid ring and electronic state, respectively. The carbon *K* edge for the benzenoid part in the epoxy resin is considered to be similar to that for aniline with a minor difference due to the presence of C_{bz}-CH_2. The spectrum for diethyl ether shows peaks as a result of excitations from 1s to Rydberg 3s, 3p states, and two σ* states.[15] The carbon *K* edge for the side-chain part in the epoxy resin is considered to be similar to that for diethyl ether with partial

modifications. The spectrum for the linear combination of aniline and diethyl ether was obtained by normalizing their intensities in the range between 282 eV and 310 eV and combining the normalized spectra in a 1:1 ratio. The experimental spectrum for D_e =0.16 has peaks at 287 eV (labeled α), 289–291 eV (labeled β), 293.5 eV (labeled γ), and 301 eV (labeled δ) in addition to peak A. The profile for D_e =0.16 is similar to the linear combination profile, although the intensities of peaks A and α are relatively lower than those of the combination spectrum. Peak A is assigned to the 1s (C_{bz}-H) → π* (e_{2u}) excitations in the benzenoid part; the excitation energy for 1s (C_{bz}-CH_2) → π* (e_{2u}) is expected to be similar to 1s (C_{bz}-H) → π* (e_{2u}) as in the case of aniline.[14, 18] The peak α can be attributed to the excitations of 1s (C_{bz} -N_{sp^3}) → π* (e_{2u}) in the benzenoid part and 1s → Rydberg 3s in the side-chain part. The peak β is mainly contributed by the excitations of 1s (C_{bz} -H) → π* (b_{2g}) and 1s (C_{bz} -N_{sp^3}) → π* (b_{2g}) in the benzenoid part and 1s → Rydberg 3p in the side-chain part. The peaks γ and δ are related to the excitation to the lower and higher σ* states in both the benzenoid and side-chain parts. According to the above considerations from Fig. 3, we find that the spectrum for D_e =0.16 at 103 K mainly reflects the chemical bonding state for the original epoxy resin before irradiation. In other words, the original structure, i.e., the chemical bonding network of carbon atoms, is maintained up to the dose of ~10^3 e^- nm^{-2} when the carbon *K* edge is probed.

C. Carbon *K* edge variation with nitrogen and oxygen *K* edges

To interpret the origin of peaks B and C that appear in the carbon *K* edge during irradiation [Fig. 2(b)], we investigated the correlations between the carbon, nitrogen, and oxygen *K* edges. Figure 4 shows the dose dependence of the carbon, nitrogen, and oxygen *K* edges obtained simultaneously from the same specimen area with j = 0.83 at 103 K. Figures 4(a) and 4(b) show exactly the same data, and the spectral colors in Fig. 4(b) correspond to those in Fig. 4(a). Figure 4(c) shows plots of the intensity for peaks B, C, D, E, and F in Figs. 4(a) and 4(c) as a function of D_e, using energy ranges of 0.7 eV for B and C, 3.5 eV for D, and 2.2 eV for E and F to obtain the integrated intensity.

For the carbon *K* edge, peaks B (at 286.6 eV) and C (at 287.4 eV) appear with increasing electron dose D_e, as shown in Fig. 2(b). Peak C begins to increase in intensity with D_e, reaches a maximum at D_e~10, and then decreases in the range $14 \leq D_e \leq 60$ in Fig. 4(c). Peak B monotonically increases with D_e up to D_e~60 in Fig. 4(c). Peak A shifts ~0.3 eV to the lower energy loss side and broadens as D_e increases from 0.5 to 60.8 without a critical decrease in intensity, as seen in Fig. 2(b). Peaks B and C can be attributed to the excitation of two π* states newly formed under electron irradiation.

For the nitrogen *K* edge, the intensity in the range of 404–410 eV is dominant at D_e =0.5. This intensity is attributed to the nitrogen 1s → σ* excitation in the original benzenoid part, demonstrating that nitrogen atoms have sp^3 states, as shown in Fig. 1(b). Then, the intensity between 397 and 400 eV with a maximum at 399.2 eV (peak D) increases rapidly up to D_e =34 followed by little change for $34 \leq D_e \leq 60$ in Fig. 4(c). Peak D and its shoulder intensities on the lower energy loss side are attributed to the excitation from 1s to the newly formed π* states (i.e., two or more π* states with close energy levels) under irradiation until D_e reaches 34. The result suggests that chemical bonds of imine (C=N) are formed, and peak B in the carbon *K* edge and peak D in the nitrogen *K* edge originate from the excitations to π* states in their sp^2 bonds.[19, 20]

For the oxygen *K* edge at D_e =0.5, there is a broadened intensity (labeled G) in the region 536–544. This intensity is attributed to the oxygen 1s → σ* excitation in the original side-chain part, demonstrating that its oxygen atoms have sp^3 states, as shown in Fig. 1(b). The intensity of G decreases up to D_e ~20 and does not change in the range $20 \leq D_e \leq 60$, as shown in Fig. 4(b). The intensity of peak F at 534.2 eV increases up to D_e ~20 and decreases in the range $20 \leq D_e \leq 60$, as shown in Fig. 4(c). The intensity variation of peak F in the oxygen *K* edge is similar to that of peak C in the carbon *K* edge. Because peaks C and F are attributed to carbon 1s → π* and oxygen 1s → π* excitations,

respectively, their correlation in intensity variation suggests that carbonyl (C=O) bonds are formed during irradiation.[19, 21, 22] This implies that sp^3-to-sp^2 conversion has occurred for oxygen atoms and their bonding carbon atoms. The intensity of peak E at 531.3 eV, which is 3 eV lower in energy than peak F, increases up to D_e ~60 in Fig. 4(c). The origin of minor peak E is not assigned in this paper.

The formation of new chemical bonds such as C=O and C=N is acceptable in terms of bond breakage and subsequent hydrogen atom loss under electron irradiation. Figure 4(b) shows that there is no critical mass loss for carbon and nitrogen atoms. For oxygen atoms, mass loss may occur only up to D_e~10 (i.e., no loss for D_e>10). Among the constituents, hydrogen atoms are most likely to cause mass loss. Because C-H bonds break more frequently in aliphatic chains than in aromatic compounds,[13] it is likely that C-H bonds in the side-chain part will break preferentially compared with C_{bz}-H in the benzenoid part for the epoxy resin. The sputtering hydrogen atoms from C-H bonds in the side-chain part can trigger the formation of new bonds such as C=O and C=N.

D. Dose-dependent EELS in the range of 1–35 eV

Figure 5 shows the variation of the EELS spectrum in the range of 1–35 eV for the epoxy resin during irradiation at 103 K. Because of the large cross section of inelastic

scattering in the low-loss region, we used a shorter exposure time (Δt=0.049) with j=0.84 to obtain the spectra at early stages of damage in the range of $D_e \leq 6.8$. The spectra for $16.3 \leq D_e \leq 399$ were obtained using Δt=0.39 and j=3.2 to observe the final profile of damaged states. At the initial stage, D_e=0.02, there is a characteristic profile in the range of 3–10 eV in addition to the plasmon energy at 22.0 eV in Fig. 5. As D_e increases, the intensities at around 4.8 eV and 6.3 eV gradually disappear and alternative broad intensity maxima appear at around 5.2 eV, while the plasmon energy gradually shifts from 22.0 eV at D_e=5.0 to 23.1 eV at D_e=399. The variation of the EELS profile in the range of 3.0–7.5 eV suggests that the primary inelastic scattering changes from $\pi \rightarrow \pi^*$ single electron transitions for D_e<5 to π-plasmon excitation for D_e>30. The intensities at ~5.2 eV and 23.1 eV at D_e=399 can be attributed to π and π+σ plasmons whose energies are similar to those in amorphous carbon.[23] A more accurate spectrum with a higher signal-to-noise ratio was obtained at the initial stage by scanning the electron beam (i.e., shifting the beam to fresh areas on the epoxy resin), acquiring low-dose EELS at 103 K, and integrating each spectrum, as shown in Fig. 6(a). There are four peaks A, B, C, and D for the epoxy resin in the range of 3.4–9.2 eV in Fig. 6(a). The local maxima for peaks A, B, C, and D are located at 3.9, 4.7, 6.0, and 6.6 eV, respectively, and the onset of intensity A is 3.5 eV. From the results of the Kramers–Kronig (K–K) analysis using the EELS

spectrum with the higher signal-to-noise ratio [Fig. 6(a)], we elucidated the real and imaginary parts, i.e., ε_1 and ε_2 of the dielectric function as shown in Fig. 6(b), and the optical absorption profile shown in Fig. 6(c). The four peaks A–D in optical absorption in Fig. 6(c) correspond to peaks A–D in EELS [Fig. 6(a)]. Figure 6(c) also shows reference optical absorption spectra of 4,4′-methylenedianiline (MDA),[24] aniline,[25] polyethylene glycol (PEG),[26] and diethyl ether.[27] The benzenoid and side-chain parts for the epoxy resin have similar structures to MDA and PEG, respectively. The characteristic peaks α, β, γ, and δ for aniline are contributed by electron excitations from π to four degeneracy-resolved π* states,[25, 28] with additional charge transfer transitions also being important components of the β and γ peaks.[28] Chemical shifts of these intensities occur depending on the type and number of functional groups in the benzenoid ring, and the shift for α and β is larger than that for γ and δ.[25, 28] Peaks α and β for MDA are located at 4.17 eV and 5.06 eV, which are lower than those for aniline.[24] For diethyl ether, the first peak ζ, at 6.35 eV originates from the excitation to the 3s Rydberg state. The peak ζ also shifts to the lower energy loss side as the ether compounds become more complex[29]. For PEG, the intensity ζ is located at 5.82 eV.[26] We consider that peaks A, B, and D are classified as α, β, and γ+δ, respectively, and originate from the benzenoid part of the epoxy resin, while peak C is classified as ζ and originates from the side-chain part. In any

case, we have successfully obtained molecular electronic transitions of the original epoxy resin by low-dose EELS at 103 K.

E. Dose-dependent ED at initial stage of irradiation

From the above-described EELS experimental results, we concluded that chemical bonding states (C-C, C-O, C-N) and molecular electronic states (π, π^*) are stable up to D_e~0.1. To investigate the effects of the initial electron irradiation around D_e=0.1, we conducted dose-dependent ED with j =8.07×10^{-4} at 103 K. Figures 7(a) and 7(b) show ED patterns with D_e=0.0005 (i.e., first acquisition) and D_e=1.211 (i.e., after irradiation for 1500 s), where the scale bars indicate the magnitude of the scattering vector, q. Although three halo rings labeled h1, h2, and h3 are visible in both Figs. 7(a) and 7(b), the intensity distribution for h1 broadens with increasing D_e. By radially rotating the ED patterns, we obtained the radially averaged ED profile with different D_e values between 0.0005 and 1.211, as in the logarithmic plots in Fig. 8(a). Figures 8(b)–8(d) show the profiles for h1, h2, and h3 after subtracting power-law fit functions from the radially averaged ED profile. The first fit ranges were 2.77–5.54 nm^{-1}, 19.7–22.4 nm^{-1}, and 36.8–39.6 nm^{-1} for h1, h2, and h3, respectively, and the second fit range was 76.1–94.6 nm^{-1} for all halo rings. Figure 8(a) shows that the peak for h1 decreases and broadens with

increasing D_e, with small shifts of the peak center from 12.9 nm^{-1} (i.e., r=0.599 nm) for D_e=0.0005 to 13.3 nm^{-1} (i.e., r=0.581 nm) for D_e=1.211, where r is the corresponding real-space distance. More specifically, r ($\approx 2.459\pi/q$) is either the interatomic, intramolecular, or intermolecular distance calculated by assigning the peaks in Figs. 8(b)–8(d) to the first maximum in the Debye scattering formula.[11, 30] The peak centers for h2 and h3 are 29.9 nm^{-1} (i.e., r= 0.258 nm) and 52.4 nm^{-1} (i.e., r= 0.147 nm), respectively, for all D_e values in Figs. 8(b) and 8(c). Figure 8(e) shows plots of normalized intensity for h1, h2, and h3 as a function of D_e, where intensities defined with integrated ranges of 8.31–17.5 nm^{-1}, 25.0–34.3 nm^{-1}, and 44.0–60.7 nm^{-1} are normalized by intensities for D_e=0.0005. It is found that h2 has a high rate of intensity decrease, while h3 has a low rate of intensity decrease.

The third halo ring (h3) with r=0.147 nm is attributed to the dominant interatomic distance (i.e., chemical bond length). The bond lengths constituting the original cured epoxy resin are expected to be approximately 0.138 nm (C_{bz}-C_{bz}), 0.142 nm (C_{bz} -N_{sp^3}), 0.147 nm (C_{sp^3}-N_{sp^3}), 0.143 nm (C_{sp^3}-O_{sp^3}), 0.108 nm (C_{bz} -H), 0.109 nm (C_{sp^3}-H), and 0.97 nm (O-H).[31] Thus, r=0.147 nm for h3 reflects the bond lengths of C-C, C-N, and C-O. During sp^3-to-sp^2 conversion, which becomes dominant for $D_e \gtrsim 20$ (Fig. 4), bond lengths can be reduced from 0.147 nm (C_{sp^3}-N_{sp^3}) to 0.128 nm (C_{sp^2}=N_{sp^2}) and from

0.143 nm (C_{sp^3}-O_{sp^3}) to 0.121 nm (C_{sp^2}=O_{sp^2}). Because there is no clear peak shift or profile change for h3 in Fig. 8(d), the sp^3 state is dominant in nitrogen and oxygen atoms at least up to D_e ~1.2, which is consistent with the EELS results in Fig. 4: the formation of C=O, C=N starts in the range $0.5 \leq D_e \leq 7.2$. The second halo ring (h2) with r= 0.258 nm is attributed to the dominant intramolecular distance, i.e., the second nearest neighbor distance between carbon, nitrogen, and oxygen atoms. The large decrease in intensity for h2 in Fig. 8(e) suggests that some bond angles, probably in the side-chain part, have changed considerably. The first halo ring (h1) with r~0.60 nm is attributed to dominant intermolecular distances characterized by benzenoid and side-chain parts in the cured epoxy resin. The decrease in peak intensity for h1 suggests that the molecular geometry of the side-chain or benzenoid parts is partially changed by deformation or rotation. The broadening of the peak for h1 suggests that the intermolecular distances have been randomized. We propose that these changes for h2 and h1, which occur simultaneously, are triggered by C-H scission,[13] which can be followed by Coulomb interaction between fast electrons and radicals at low temperatures. The results of dose-dependent ED indicate that changes in molecular geometry dominate at intramolecular and intermolecular length scales (i.e., ~0.26 nm and ~0.60 nm).

F. Damage mechanism

Figure 9 illustrates a possible damage mechanism of the cured epoxy resin by the fast electrons at low temperatures derived from the above experimental results, in terms of molecular structure (upper figure) and π-electron distribution (lower figure). Before electron irradiation, nitrogen and oxygen atoms form sp^3 states for their chemical bonding, and the π-electron exists only on the benzenoid ring. At the initial stage of irradiation ($D_e \lesssim 0.1$), C-H scissions and subsequent Coulomb interactions between radicals and fast electrons can change the intramolecular geometry, such as the bond angles in the side-chain part, and also the intermolecular geometry (geometry between two benzenoid parts, between two side-chain parts, and between benzenoid and side-chain parts). In the range $0.5 \lesssim D_e \lesssim 10$, nitrogen and oxygen atoms change from sp^3 to sp^2 states, and the sp^2 state of carbon also increases, implying the formation of C=O and C=N bonds in the epoxy resin, as illustrated in Fig. 9. Sputtering hydrogen atoms of -OH and its adjacent -CH can form the C=O bond, while breaking a C-N bond and a sputtering hydrogen atom of -CH adjacent to nitrogen atom can form the C=N bond. The mechanism in Fig. 9 implies that π-electrons, initially present only at the benzenoid ring, also become present in the side-chain part, resulting in an increase in π-electron density throughout the epoxy resin. Furthermore, as a result of the sputtering hydrogen atom of -CH_2 between two benzenoid

rings (Fig. 1), the benzenoid rings can be connected and the π-electrons can become spatially continuous. The increase in π-electron density with D_e is consistent with the result in Fig. 5, where a predominant excitation changes from π→π* transitions (i.e., single-electron excitation) to π-plasmon excitation (i.e., collective oscillation of the charge distribution spread in real space by excited π-electrons) in the range of 3.0–7.5 eV with increasing D_e. At the final stage of damage ($D_e \gtrsim 100$), the profiles for 1s →σ* in the carbon *K* edge in the range of 290–305 eV in Fig. 5 are analogous to those of amorphous carbon,[32] and the π-plasmon is relatively intense in Fig. 5. This suggests that the fully damaged epoxy resin ($D_e \gtrsim 100$) has a disordered structure mainly consisting of carbon atoms with small numbers of nitrogen and oxygen atoms.[23] Although the disordered structure can partially have graphitic structures as a result of the joining of the benzenoid rings, the presence of carbon and oxygen atoms prevents the fully damaged epoxy resin from having a complete graphite-like honeycomb structure.[33-35]

IV. CONCLUSION

The damage mechanism and exposure tolerance of epoxy resin (i.e., TGMDA as the base resin) to fast electrons were quantitatively investigated by dose-dependent EELS and ED. It was found that the sp^3 states of nitrogen, oxygen, and their adjacent carbon atoms

changed to sp^2 states, forming C=N and C=O, as the total electron dose increased at 103 K. The sputtering hydrogen atoms and the breaking of C-H bonds by the fast electrons can cause the sp^3-to-sp^2 conversion. It was proposed that the fully damaged epoxy resin has a disordered structure with partially graphitized structures. The epoxy resin was very sensitive to fast electrons, and the original electronic states were maintained at 103 K up to a total dose of ~10^3 e^- nm^{-2}. Below this dose limit, we were able to measure electronic states in the ultraviolet region by EELS with the high DQE camera. Intra- and intermolecular geometry changes below and around the total dose of ~10^3 e^- nm^{-2} were also observed by ED. The results obtained in this study provide important information for the electron microscopic analysis of various epoxy resins and other polymeric materials. The results are also important from the viewpoint of durability and mechanisms of the degradation of epoxy resins by fast charged particles in special environments such as space.

ACKNOWLEDGMENTS

J.K. thanks O. Cretu and N. Kawamoto (NIMS) for their insightful comments.

AUTHOR DECLARATIONS

Conflict of Interest

The authors have no conflicts to disclose.

Author Contributions

A.N. and Y.S. prepared the specimens. A.N. and J.K. conducted EELS and ED experiments. All authors discuss the experimental results. J.K. wrote the manuscript with the support of all the authors.

DATA AVAILABILITY

The data that support the findings of this study are available within this article

REFERENCES

[1] J. C. Capricho, B. Fox, and N. Hameed, Polymer Reviews **60**, 1–41 (2020)..

[2] A. Paillous, and C. Pailler, Composite **25**, 287–295 (1994).

[3] A. Shundo, S. Yamamoto, and K. Tanaka, JACS Au **2**, 1522–1542 (2022).

[4] T. Hoshino, Y. Okamoto, A. Yamamoto, and H. Masunaga, Sci. Rep. **11**, 9767 (2021).

[5] S. Horiuchi, Y. Liu, T. Hanada, and H. Akiyama, Appl. Surf. Sci. **599**, 153964 (2022).

[6] G. Haberfehlner, S. F. Hoefler, T. Rath, G. Trimmel, G. Kothleitner, and F. Hofer, Micron **140**, 102981 (2021).

[7] R. Colby, R. E. A. Williams, D. L. Carpenter, N. Bagués, B. R. Ford, and D. W. McComb, Ultramicroscopy **246**, 113688 (2023).

[8] T. Sasuga, and A. Udagawa, Polymer **32**, 402–408 (1991).

[9] G. Yu, D. Shangli, Y. Dezhuang, H. Shiyu, and L. Zhijun, J. Polym. Sci., Part B: Polym. Phys. **44**, 177–184 (2006).

[10] W. Zhang, L. G. d. A. Melo, A. P. Hitchcock, and N. Bassim, Micron **120**, 74–79 (2019).

[11] K. Yoshida, H.-H. Huang, T. Miyata, Y. K. Sato, and H. Jinnai, Microscopy **72**, 361–367 (2022).

[12] R. F. Egerton, *Electron energy-loss spectroscopy in the electron microscope*, Third ed. (Springer, New York, 2011).

[13] L. Reimer, and H. Kohl, *Transmission Electron Microscopy*, Fifth ed. (Springer, New York, 2007).

[14] C. C. Turci, S. G. Urquhart, and A. P. Hitchcock, Can. J. Chem. **74**, 851–869 (1996).

[15] S. G. Urquhart, A. P. Hitchcock, R. D. Priester, and E. G. Rightor, J. Polym. Sci., Part B: Polym. Phys. **33**, 1603–1620 (1995).

[16] Y. Joseph, M. Wühn, A. Niklewski, W. Ranke, W. Weiss, C. Wöll, and R. Schlögl, Phys. Chem. Chem. Phys. **2**, 5314–5319 (2000).

412 [17] D. Duflot, J. P. Flament, A. Giuliani, J. Heinesch, M. Grogna, and M. J. Hubin-
413 Franskin, Phys. Rev. A **75**, 052719 (2007).
414 [18] S. G. Urquhart, A. P. Hitchcock, A. P. Smith, H. W. Ade, W. Lidy, E. G. Rightor, and
415 G. E. Mitchell, J. Electron. Spectrosc. Relat. Phenom. **100**, 119–135 (1999).
416 [19] J. Alleon, S. Bernard, C. L. Guillou, O. Beyssac, K. Sugitani, and F. Robert,
417 Geochem. Perspect. Lett. **7**, 37–42 (2018).
418 [20] H. Yabuta, M. Uesugi, H. Naraoka, M. Ito, A. L. D. Kilcoyne, S. A. Sandford, F.
419 Kitajima, H. Mita, Y. Takano, T. Yada, Y. Karouji, Y. Ishibashi, T. Okada, and M. Abe,
420 Earth, Planets and Space **66**, 156 (2014).
421 [21] K. Varlot, J. M. Martin, C. Quet, and Y. Kihn, Ultmicroscopy **68**, 123–133 (1997).
422 [22] A. P. Hitchcock, S. G. Urquhart, and E. G. Rightor, J. Phys. Chem **96**, 8736–8750
423 (1992).
424 [23] S. Bhattacharyya, C. Vallée, C. Cardinaud, O. Chauvet, and G. Turban, J. Appl. Phys.
425 **85**, 2162–2169 (1999).
426 [24] E. Mohseni, M. R. Yaftian, H. Shayani-jam, A. Zamani, and F. Piri, Iran. Polym. J.
427 **29**, 403–409 (2020).
428 [25] K. Kimura, H. Tsubomura, and S. Nagakura, Bull. Chem. Soc. Jpn. **37**, 1336–1346
429 (1964).

[26] M. Todica, O. Stan, C. V. Pop, Ş. Răzvan, and C. Niculăescu, Rom. J. Phys. **65**, 702 (2020).

[27] R. K. Burdick, J. P. Villabona-Monsalve, G. A. Mashour, and T. Goodson, Sci. Rep. **9**, 11351 (2019).

[28] T. Ari, H. Güven, and N. Ecevit, J. Electron. Spectrosc. Relat. Phenom. **73**, 13–23 (1995).

[29] Q. Y. Shang, P. O. Moreno, R. Disselkamp, and E. R. Bernstein, J. Chem. Phys. **98**, 3703–3712 (1993).

[30] P. Debye, Ann. Phys. **351**, 809–823 (1915).

[31] A. G. Orpen, L. Brammer, F. H. Allen, O. Kennard, D. G. Watson, and R. Taylor, Appendix A in *Structure Correlation* (VCH Verlagsgesellschaft mbH, Weinheim, 1994), pp. 752–858.

[32] F. Langenhorst, and V. L. Solozhenko, Phys. Chem. Chem. Phys. **4**, 5183–5188 (2002).

[33] D. Ugarte, Nature **359**, 707–709 (1992).

[34] M. Chhowalla, H. Wang, N. Sano, K. B. K. Teo, S. B. Lee, and G. A. J. Amaratunga, Phys. Rev. Lett. **90**, 155504 (2003).

[35 1] J. C. Capricho, B. Fox, and N. Hameed, Polymer Reviews **60**, 1–41 (2020).

[2] A. Paillous, and C. Pailler, Composite **25**, 287–295 (1994).

[3] A. Shundo, S. Yamamoto, and K. Tanaka, JACS Au **2**, 1522–1542 (2022).

[4] T. Hoshino, Y. Okamoto, A. Yamamoto, and H. Masunaga, Sci. Rep. **11**, 9767 (2021).

[5] S. Horiuchi, Y. Liu, T. Hanada, and H. Akiyama, Appl. Surf. Sci. **599**, 153964 (2022).

[6] G. Haberfehlner, S. F. Hoefler, T. Rath, G. Trimmel, G. Kothleitner, and F. Hofer, Micron **140**, 102981 (2021).

[7] R. Colby, R. E. A. Williams, D. L. Carpenter, N. Bagués, B. R. Ford, and D. W. McComb, Ultramicroscopy **246**, 113688 (2023).

[8] T. Sasuga, and A. Udagawa, Polymer **32**, 402–408 (1991).

[9] G. Yu, D. Shangli, Y. Dezhuang, H. Shiyu, and L. Zhijun, J. Polym. Sci., Part B: Polym. Phys. **44**, 177–184 (2006).

[10] W. Zhang, L. G. d. A. Melo, A. P. Hitchcock, and N. Bassim, Micron **120**, 74–79 (2019).

[11] K. Yoshida, H.-H. Huang, T. Miyata, Y. K. Sato, and H. Jinnai, Microscopy **72**, 361–367 (2022).

[12] L. Reimer, and H. Kohl, *Transmission Electron Microscopy*, Fifth ed. (Springer Science+Business Media, LLC, New York, 2007).

[13] C. C. Turci, S. G. Urquhart, and A. P. Hitchcock, Can. J. Chem. **74**, 851–869 (1996).

[14] S. G. Urquhart, A. P. Hitchcock, R. D. Priester, and E. G. Rightor, J. Polym. Sci., Part B: Polym. Phys. **33**, 1603–1620 (1995).

[15] Y. Joseph, M. Wühn, A. Niklewski, W. Ranke, W. Weiss, C. Wöll, and R. Schlögl, Phys. Chem. Chem. Phys. **2**, 5314–5319 (2000).

[16] D. Duflot, J. P. Flament, A. Giuliani, J. Heinesch, M. Grogna, and M. J. Hubin-Franskin, Phys. Rev. A **75**, 052719 (2007).

[17] S. G. Urquhart, A. P. Hitchcock, A. P. Smith, H. W. Ade, W. Lidy, E. G. Rightor, and G. E. Mitchell, J. Electron. Spectrosc. Relat. Phenom. **100**, 119–135 (1999).

[18] J. Alleon, S. Bernard, C. L. Guillou, O. Beyssac, K. Sugitani, and F. Robert, Geochem. Perspect. Lett. **7**, 37–42 (2018).

[19] H. Yabuta, M. Uesugi, H. Naraoka, M. Ito, A. L. D. Kilcoyne, S. A. Sandford, F. Kitajima, H. Mita, Y. Takano, T. Yada, Y. Karouji, Y. Ishibashi, T. Okada, and M. Abe, Earth, Planets and Space **66**, 156 (2014).

[20] K. Varlot, J. M. Martin, C. Quet, and Y. Kihn, Ultmicroscopy **68**, 123–133 (1997).

[21] A. P. Hitchcock, S. G. Urquhart, and E. G. Rightor, J. Phys. Chem **96**, 8736–8750 (1992).

[22] S. Bhattacharyya, C. Vallée, C. Cardinaud, O. Chauvet, and G. Turban, J. Appl. Phys. **85**, 2162–2169 (1999).

[23] E. Mohseni, M. R. Yaftian, H. Shayani-jam, A. Zamani, and F. Piri, Iran. Polym. J. **29**, 403–409 (2020).

[24] K. Kimura, H. Tsubomura, and S. Nagakura, Bull. Chem. Soc. Jpn. **37**, 1336–1346 (1964).

[25] M. Todica, O. Stan, C. V. Pop, Ş. Răzvan, and C. Niculăescu, Rom. J. Phys. **65**, 702 (2020).

[26] R. K. Burdick, J. P. Villabona-Monsalve, G. A. Mashour, and T. Goodson, Sci. Rep. **9**, 11351 (2019).

[27] T. Ari, H. Güven, and N. Ecevit, J. Electron. Spectrosc. Relat. Phenom. **73**, 13–23 (1995).

[28] Q. Y. Shang, P. O. Moreno, R. Disselkamp, and E. R. Bernstein, J. Chem. Phys. **98**, 3703–3712 (1993).

[29] P. Debye, Ann. Phys. **351**, 809–823 (1915).

[30] A. G. Orpen, L. Brammer, F. H. Allen, O. Kennard, D. G. Watson, and R. Taylor, Appendix A in *Structure Correlation* (VCH Verlagsgesellschaft mbH, Weinheim, 1994), pp. 752–858.

[31] F. Langenhorst, and V. L. Solozhenko, Phys. Chem. Chem. Phys. **4**, 5183–5188 (2002).

[32] D. Ugarte, Nature **359**, 707–709 (1992).

[33] M. Chhowalla, H. Wang, N. Sano, K. B. K. Teo, S. B. Lee, and G. A. J. Amaratunga, Phys. Rev. Lett. **90**, 155504 (2003).

[34] D. Lungerich, H. Hoelzel, K. Harano, N. Jux, K. Y. Amsharov, and E. Nakamura, ACS Nano **15**, 12804–12814 (2021).

508 **Figures**

509

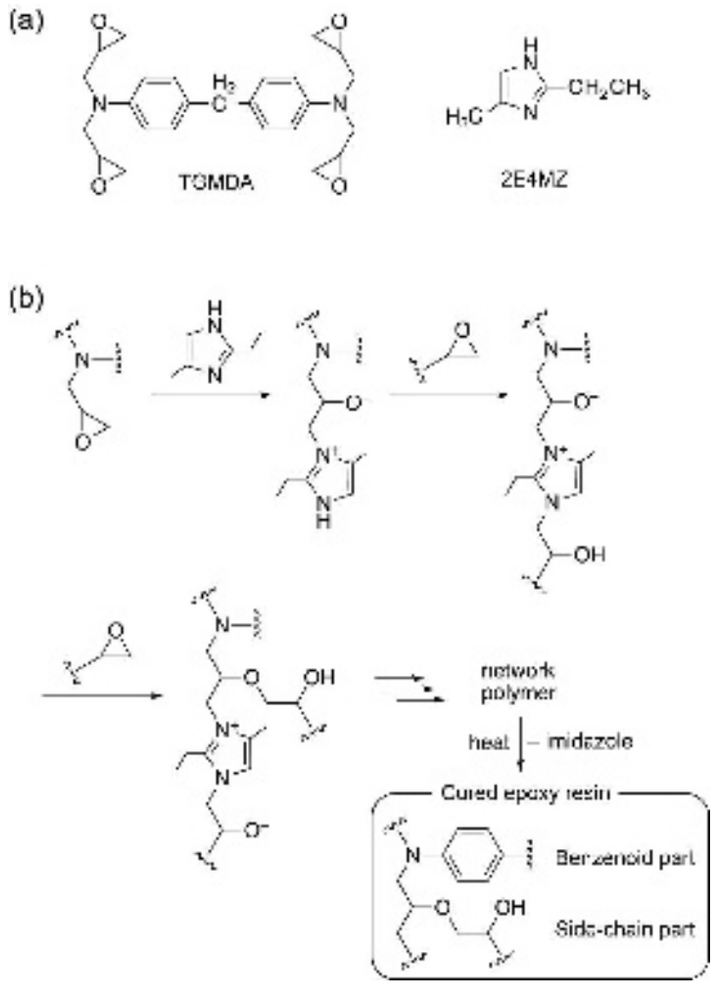

510

511

512 **FIG. 1.** (a) Monomers of TGMDA and 2E4MZ as base resin and curing agent,

513 respectively. (b) Possible curing reaction sequence. Polymerization by alternative ring-

514 opening and chain-growth processes followed by thermal detachment of 2E4MZ yields

515 the final cured epoxy resin composed of benzenoid and side-chain parts.

516

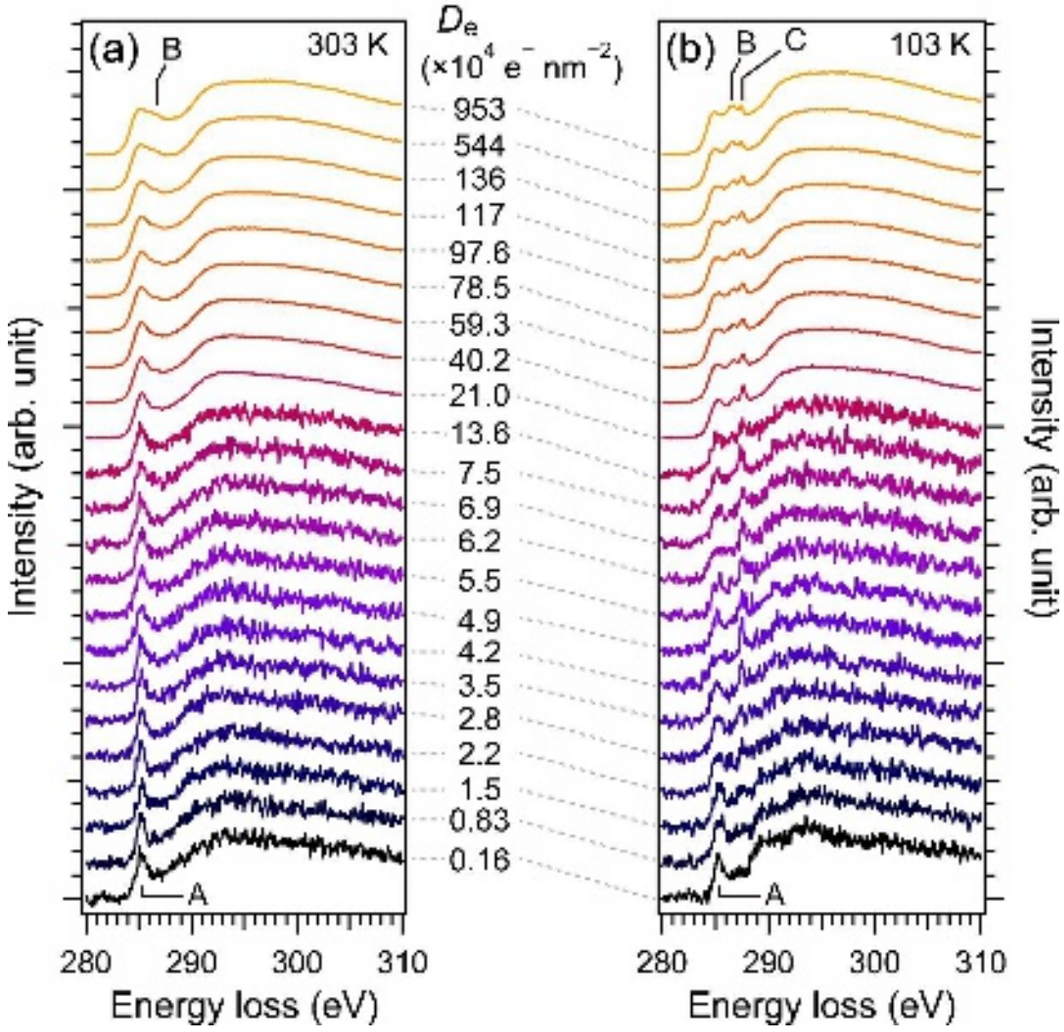

FIG. 2. Changes in carbon *K* edges for the epoxy resin with total electron dose D_e at (a) 303 K and (b) 103 K.

522

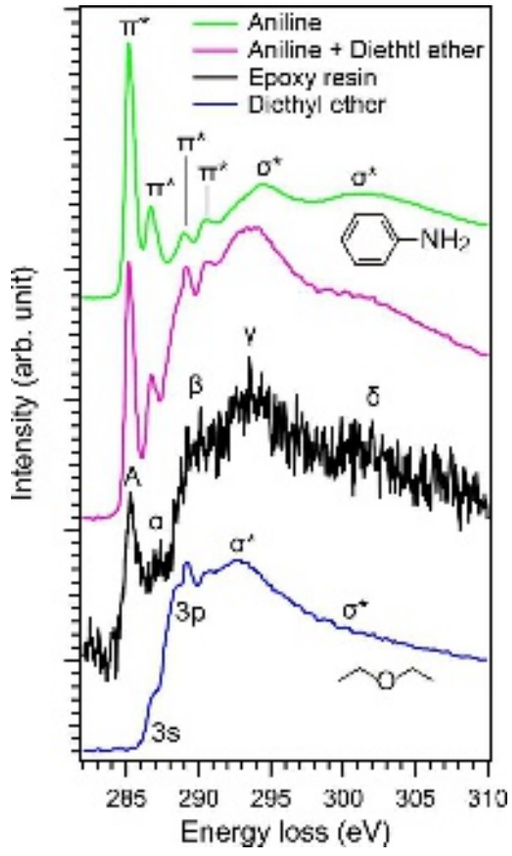

523

524

525 **FIG. 3.** Carbon *K* edges of the epoxy resin for D_e=0.16 at 103 K in Fig. 2(b), with

526 aniline,[14] diethyl ether,[15] and the linear combination profile of aniline and diethyl ether.

527

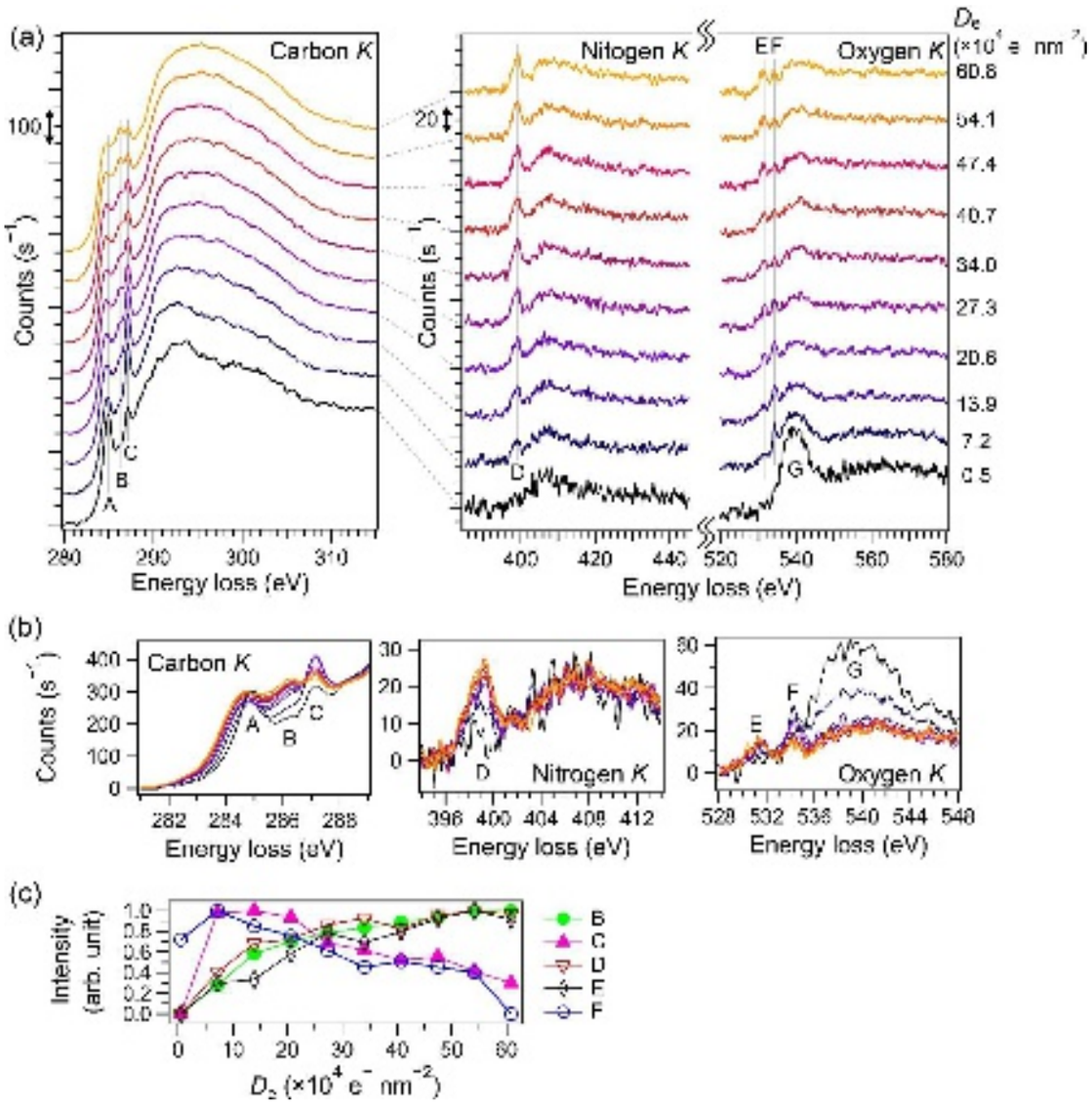

FIG. 4. Simultaneously acquired carbon, nitrogen, and oxygen *K* edges for the epoxy resin as D_e increases, shown in (a) array and (b) overlay. (c) Intensity changes for B–F with D_e.

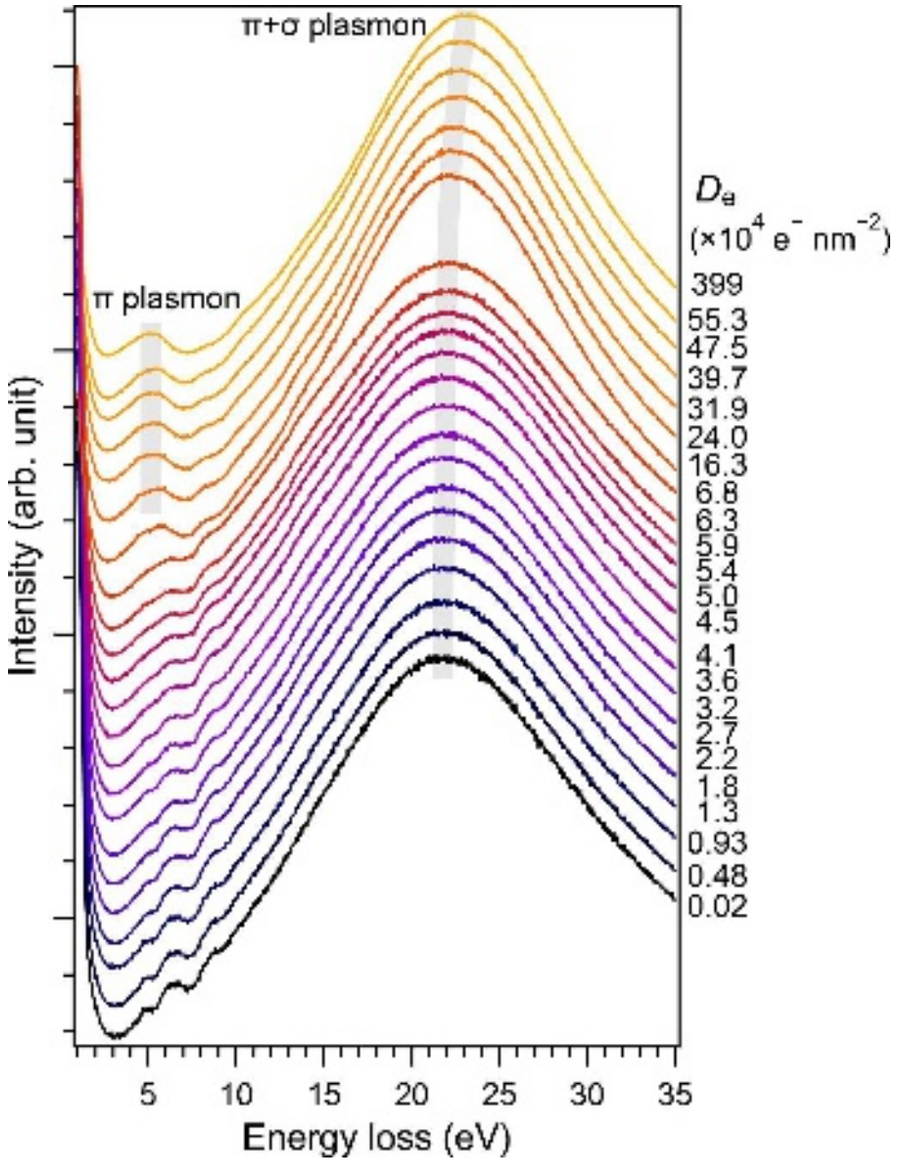

FIG. 5. Change in EELS spectrum for the epoxy resin at 103 K in the range of 1–35 eV with total electron dose D_e.

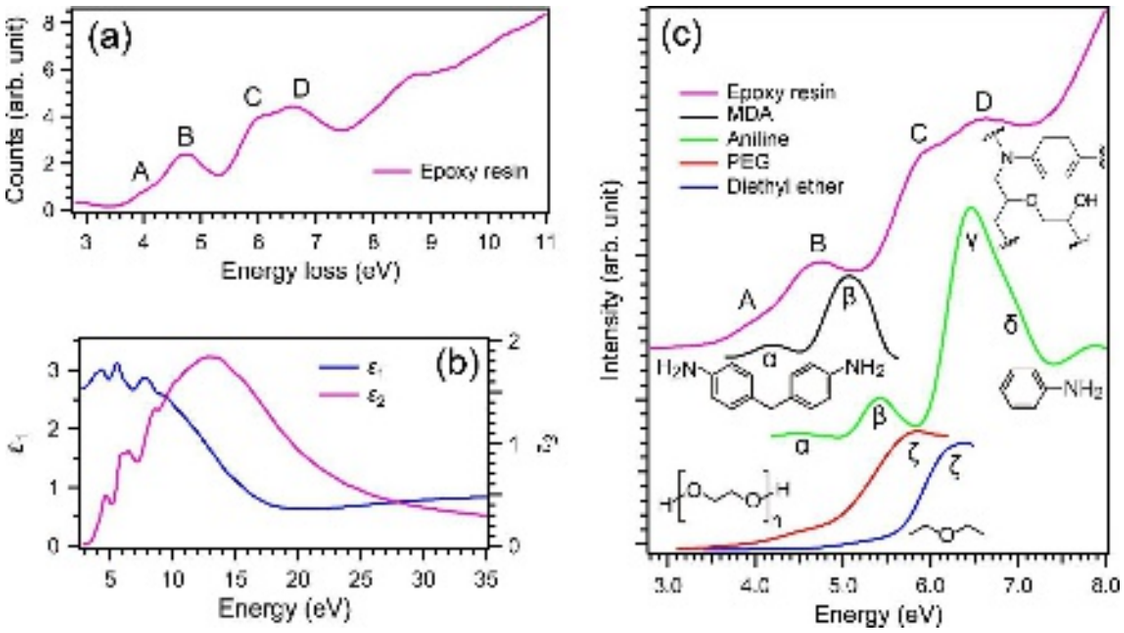

FIG. 6. (a) High signal-to-noise ratio EELS spectrum for the epoxy resin at 103 K with a dose equivalent to D_e~0.01 with reference EELS. (b) Real (ε_1) and imaginary (ε_2) parts of the dielectric function derived by K–K analysis for the EELS spectrum of D_e~0.01 in (a). (c) Optical absorption profile of the epoxy resin obtained by K–K analysis using the EELS spectrum in (a), with optical absorption spectra of 4,4′-methylenedianiline (MDA),[24] aniline,[25] polyethylene glycol (PEG),[26] and diethyl ether.[27]

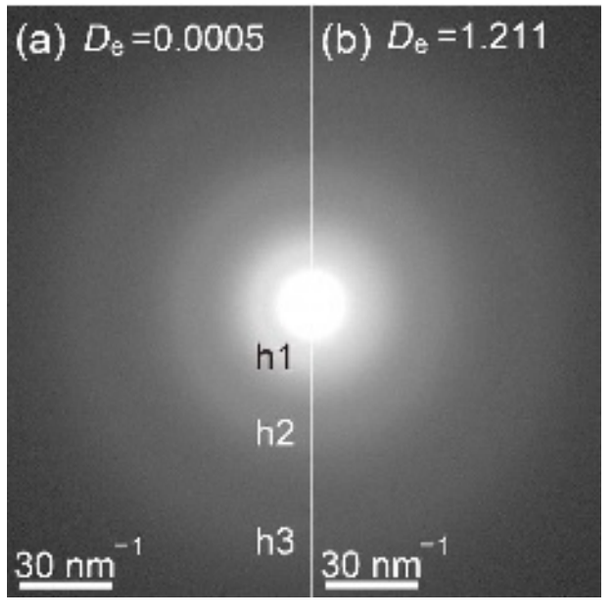

FIG. 7. ED pattern of the epoxy resin at 103 K with total electron dose D_e values of (a) 0.0005 and (b) 1.211. The scale is in the magnitude of the scattering vector.

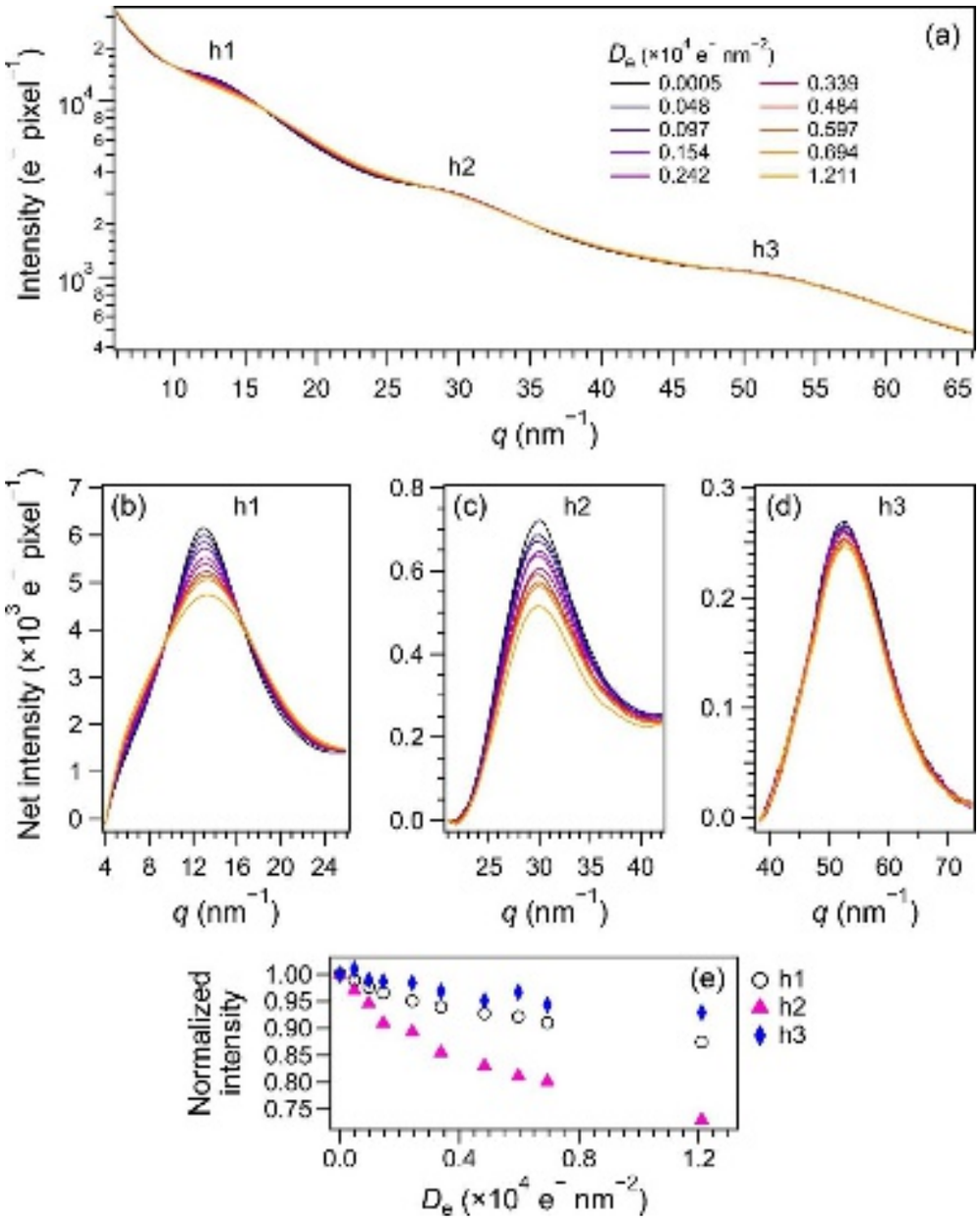

FIG. 8. (a) Logarithmic plot of the radially averaged ED patterns [Figs. 7(a), 7(b), and others (not shown)] of the epoxy resin at 103 K with different total electron dose D_e values. Net intensity profiles after subtraction of background intensity for (b) h1, (c) h2, and (d) h3 with different total electron dose D_e values as indicated in (a). (e) Normalized intensities of h1, h2, and h3 as a function of D_e.

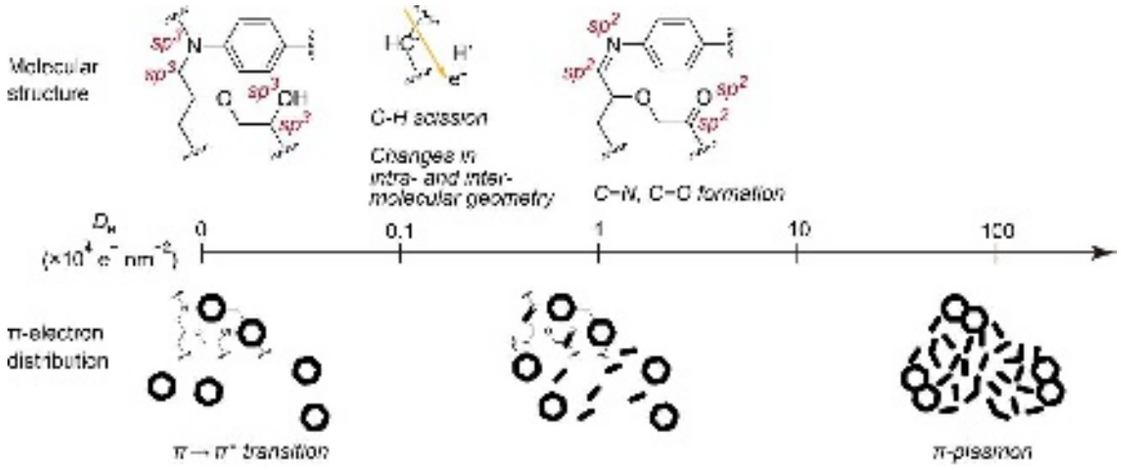

FIG. 9. Damage mechanism of the epoxy resin by fast electrons from the viewpoint of molecular structure (upper figure) and π-electron distribution (lower figure). The sp^3-to-sp^2 conversion for nitrogen, oxygen, and their adjacent carbon atoms follows the C-H scission and changes in intra- and intermolecular geometries (upper figure). The initially isolated π-electrons become dense (lower figure), allowing π-plasmon excitation.